Article

Antimony- and Zinc-Doped Tin Oxide Shells Coated on Gold Nanoparticles and Gold−Silver Nanoshells Having Tunable Extinctions for Sensing and Photonic Applications

Riddhiman Medhi, Chien-Hung Li, Sang Ho Lee, Pannaree Srinoi, Maria D. Marquez, Francisco Robles-Hernandez, Allan J. Jacobson, Tai-Chou Lee, and T. Randall Lee*

ACCESS | Metrics & More | Article Recommendations | SI Supporting Information

ABSTRACT: This paper reports the synthesis and study of doped metal oxides as the shell in core−shell nanoparticle architectures. Specifically, the paper describes the synthesis of gold nanoparticles (Au NPs) and gold−silver nanoshells (GS-NSs) coated with antimony- and zinc-doped tin oxide (SnO_2) shells (i.e., Au@ATO, Au@ZTO, GS-NS@ATO, and GS-NS@ZTO) with a comparison to the undoped SnO_2-coated analogues Au@SnO_2 and GS-NS@SnO_2. The doped tin oxide core−shell nanoparticles prepared here were thoroughly characterized using scanning electron microscopy, transmission electron microscopy, dynamic light scattering, energy-dispersive X-ray spectroscopy, X-ray photoelectron spectroscopy, and X-ray diffraction. Separately, their optical properties were evaluated by UV−vis and photoluminescence spectroscopy. The results demonstrate that noble-metal nanoparticles such as Au NPs and GS-NSs, which exhibit strong surface plasmon resonances at visible-to-near-IR wavelengths, can be activated across a broader region of the solar spectrum when used in conjunction with wide-band-gap semiconductors. In particular, utilization of a GS-NS core induces near-complete suppression in the electron−hole recombination processes in the tin oxide materials. Potential impacts on sensing and photonic applications are highlighted.

KEYWORDS: core−shell nanoparticles, doped tin oxide shells, gold−silver nanoshells, localized surface plasmon resonance, antimony-doped, zinc-doped

INTRODUCTION

Metal oxide nanoparticles are widely used for acoustic devices, solar cells, gas sensors, piezoelectric devices, thin-film transistors, textiles, rubber products, light-emitting diodes, laser diodes, chemical sensors, biosensors, and as antibacterial and antifungal agents.[1−7] While doping is an effective strategy for enhancing the optical and electrical properties of metal oxides,[7−10] it also enhances the reactivity of metal oxide surfaces; consequently, the synthesis of stable and uniform doped metal oxide nanoparticles is a challenge for most researchers.[11,12] Nevertheless, a few groups have developed effective methods for the preparation of uniform and monodisperse doped metal oxide nanoparticles.[13−15] However, because of the difficulties caused by the surface reactivity upon doping, the synthesis of doped metal oxides as the shell in core−shell nanoparticle architectures is a largely understudied field. Recently, Milliron and co-workers reported the synthesis of tin-doped indium oxide (ITO) shells around indium oxide cores.[13] However, to the best of our knowledge, there are no reports describing the growth of uniform doped metal oxide shells on different types of material cores (e.g., a metallic,

polymeric, or silica nanoparticle core). This report describes the synthesis of uniformly doped tin oxide shells on plasmonic metal cores.

Tin oxide (SnO_2), an n-type semiconductor with a wide band gap (E_g = 3.6 eV at 300 K),[16] has gained increasing importance for applications such as gas sensors,[17] solar cells,[18] and transistors.[19] In addition, tin oxide is widely used in the fabrication of thin films for transparent conducting electrodes.[20] The photocatalytic activity of SnO_2-based materials has also attracted attention because of attractive carrier properties and stability across a wide range of pH values.[21] The chemical and physical properties of SnO_2-based materials can be markedly enhanced by introducing a wide range of dopants. For example, ITO,[22] fluorine-doped tin oxide (FTO),[23]
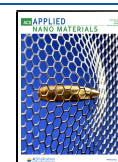
Scheme 1. Synthesis Routes Used to Prepare SnO$_2$-, ATO-, and ZTO-Coated Au NPs and GS-NSs
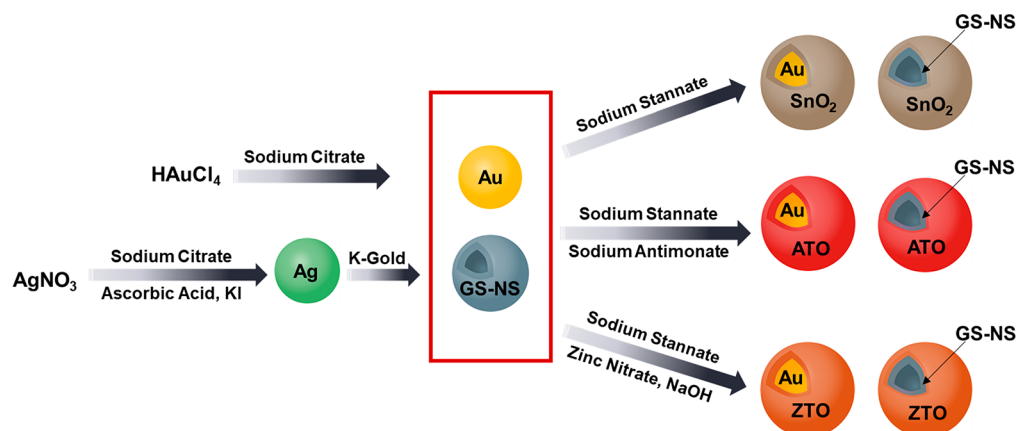
tungsten-doped tin oxide (WTO),[24] antimony-doped tin oxide (ATO),[25] and zinc-doped tin oxide (ZTO)[26] are widely used as transparent conducting oxide materials. The most commonly employed doped SnO$_2$ material is ITO, which consists of 90% In$_2$O$_3$ and 10% SnO$_2$. ITO has found widespread use in flat-panel display technologies because of its excellent conductivity. However, the high cost associated with indium oxide has led to a demand for cost-effective replacements. ATO and ZTO have emerged as perhaps the two most promising alternatives, demonstrating high conductivities that are slightly lower than that of ITO but at only a fraction of the cost. ATO and ZTO have high carrier mobilities along with excellent optical transmittance; moreover, they are also chemically and thermally more stable than undoped SnO$_2$.[10,25−27]

Despite these attractive characteristics, a major drawback of SnO$_2$-based materials is that, because of their large band gap, their optical responses are limited to the UV region, which limits their utilization to only 5% of the solar spectrum reaching the surface of the earth.[28] Doping and coupling with plasmonic conjugates are two strategies that researchers have used to broaden the optical absorption of metal oxide nanoparticle systems. In particular, ATO nanoparticles exhibit enhanced absorption of visible light compared to undoped tin oxide nanoparticles;[15] furthermore, the use of plasmonic metal nanoparticles as cocatalysts has enabled photocatalytic activity of metal oxide nanoparticles in the visible region of the solar spectrum.[29] A cost-effective strategy for the latter method involves the use of hollow alloy nanoshell particles,[30] which afford broad localized surface plasmonic resonances (LSPRs) and require only small amounts of noble metals.

The rapid recombination of photogenerated electrons and holes is another major drawback associated with traditional metal oxides because this process decreases the quantum efficiency.[31,32] Plasmonic gold nanoparticles (Au NPs) have been used to reduce electron−hole recombination in tin oxide nanostructures, thus enhancing the photocatalytic activity of SnO$_2$ materials.[33,34] In these instances, the excited electrons transfer from the conduction band of the photocatalyst onto the Au NPs, thereby trapping them and slowing their recombination.[34] We envision that plasmonic cores in the form of Au NPs or gold−silver nanoshells (GS-NSs) embedded within a semiconductor photocatalyst shell might give rise to a similar quenching of electron−hole recombination. Thus, to expand the optical properties of tin oxide nanomaterials to other regions of the solar spectrum and

reduce the electron−hole recombination process in these metal oxides, our current research seeks to prepare and study plasmonic cores in the form of Au NPs and GS-NSs coated with doped and undoped nanoscale tin oxide shells as reported here.

In addition to photovoltaic and photocatalytic applications, tin oxide materials are important components of gas sensors along with other metal oxides such as ZnO, TiO$_2$, In$_2$O$_3$, WO$_3$, CuO, and Fe$_2$O$_3$.[35] Tin oxide materials have demonstrated the capacity to sense CO, CO$_2$, NO$_x$, combustible gases (H$_2$ and methane), hydrocarbons (methane), volatile organic compounds (such as benzene, toluene, chloroform, and octane), and toxic gases (ammonia).[35−37] The key structural factors that determine the sensitivity of tin oxide sensors are the porosity and grain size.[38,39] The sensing activity increases with decreasing grain size until ∼6 nm, which is double the thickness of the space-charge layer in tin oxide.[39,40] Typically, the fabrication of tin oxide and doped tin oxide thin films involves annealing, which leads to grain growth and decreasing porosity, both of which limit sensitivity, especially at ambient temperatures.[39]

Recently, household gas sensors have become important for monitoring the air quality in homes and office buildings. In contrast to industrial gas sensors, which operate at high temperatures, household gas sensors should be designed to function at room temperature. There have been a few reports that have utilized noble-metal nanoparticles in combination with metal oxides to enhance the sensing efficiency.[36,39,41] Au NPs can act as a catalyst to absorb the gases and activate sensing in nearby tin oxide nanoparticles;[38,42] however, having the noble-metal nanoparticles seeded on the surface of the metal oxide makes them unstable to sintering, limits molecular access to the metal oxide surface, and makes them vulnerable to contamination, all of which lead to diminished catalytic activity.[37] Yu and Dutta first noted the ability of an Au@SnO$_2$ core−shell nanostructure to lower the operating temperature of SnO$_2$ gas sensors.[39] Complementary research conducted by Wu and co-workers found that both silver nanoparticle (Ag NP) and Au NP cores can enable tin oxide shells to sense gases such as formaldehyde, ethanol, and carbon monoxide (CO) at room temperature.[36,41] While exploiting the strong LSPR properties of noble-metal nanoparticles can also enhance the light-activated gas sensing in metal oxides,[43] doping can add additional enhancements to the sensing properties of tin oxides.[35,44] Notably, antimony doping in tin oxide sensors creates a material resistant to hydroxyl poisoning induced by
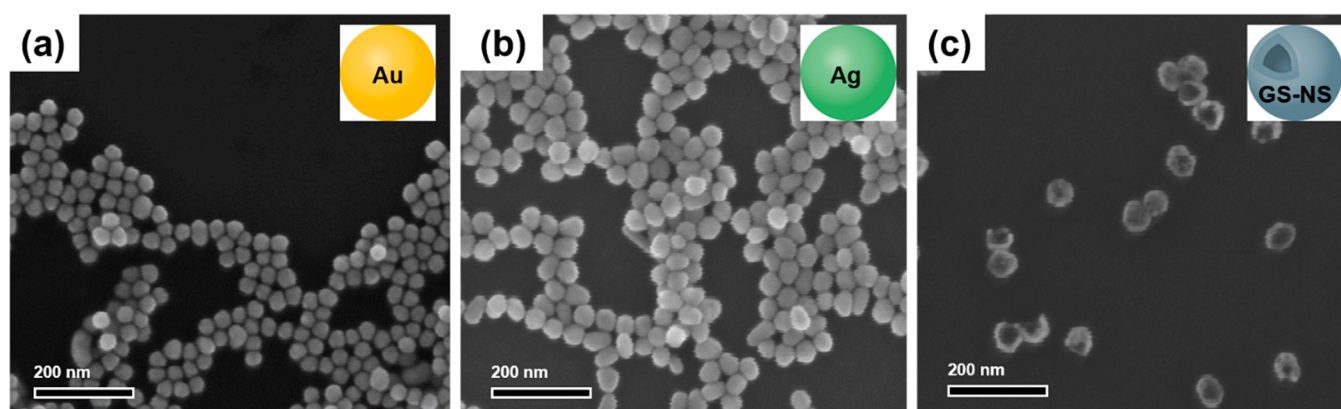
Figure 1. SEM images of (a) Au NPs, (b) Ag NPs, and (c) GS-NSs, respectively.

humidity;[45] moreover, ATO has been used to sense CO, ethanol, ammonia, and chlorine.[35]

When analyzed broadly, previous studies indicate multiple advantages of combining doped tin oxide shells with plasmonic gold and gold–silver alloy cores for both photocatalytic and sensing applications. However, in spite of these indicators, plasmonic cores coated with doped metal oxide shells are, to the best of our knowledge, yet to be studied, primarily because of the difficulties associated with the synthesis of such nanomaterials. In this report, we describe reproducible synthetic routes to these promising nanoarchitectures, which should offer substantial functional advantages over existing hybrids of metal oxides and Au NPs.

■ EXPERIMENTAL SECTION

The materials, characterization methods, and synthetic procedures and parameters used to synthesize the gold nanoparticles (Au NPs), gold–silver nanoshells (GS-NSs), antimony- or zinc-doped tin oxide shell-coated plasmonic cores (Au@ATO, Au@ZTO, GS-NS@ATO, and GS-NS@ZTO), and bare SnO_2-coated analogues (Au@SnO_2 and GS-NS@SnO_2) are detailed in the Supporting Information (Table S1 and Figures S1–S18).

■ RESULTS AND DISCUSSION

Synthesis and Morphological Characterization of the Nanoparticles. *Au NPs and GS-NSs.* The strategy used to prepare Au NPs and hollow GS-NSs is outlined in Scheme 1 and detailed in the Supporting Information. Au NPs are the most widely used plasmonic nanoparticle across multiple research groups as well as in industry; consequently, it was important to develop a methodology for coating Au NPs with doped tin oxide shells. Strategies for preparing stable and well-defined Au NPs are many, affording discrete nanomaterials that are plasmonically active in the visible region.[46] Au NPs with dimensions of around 10–15 nm can be readily prepared using chloroauric acid as the gold source and sodium citrate as the reducing agent. We used two slight variations of this method to prepare Au NPs for (a) coating with SnO_2 shells and (b) coating with ATO and ZTO shells, described in the Supporting Information as Route A and Route B, respectively. Minor variations were used to optimize the concentrations in the tin oxide coating step, described in the next section. The Au NPs were uniform and spherical, as is evident from Figure 1a. As determined by dynamic light scattering (DLS; see below), the average hydrodynamic diameter of the Au NPs was 15 ± 5 nm.

GS-NSs were prepared in two steps, as described in Scheme 1.[30] First, Ag NPs having diameters of ∼60−80 nm were prepared from a silver nitrate solution [see the scanning electron microscopy (SEM) images in Figure 1b].[31,47] To circumvent the coformation of silver nanorods, it is important to add potassium iodide and ascorbic acid to the reaction mixture, with careful control of the concentration and temperature throughout the course of the reaction. In the present study, the concentration of potassium iodide was judiciously adjusted from the previous recipes in an effort to yield consistently and exclusively spherical Ag NPs. We note also that the round-bottomed flask and stir bar used for the synthesis of Ag NPs were washed twice with aqua regia before every reaction. Furthermore, the condenser was thoroughly cleaned and rinsed with Milli-Q water, and the stirring speed was maintained at 600 rpm. Using these protocols, we obtained uniform spherical Ag NPs with no rods, as demonstrated in Figure 1b. With regard to the reproducibility, the methodology reported here yields uniform spherical silver particles at least 8 out of every 10 times, with little or no contamination by silver nanorods.

Once the Ag NPs were obtained, we treated them with a K-gold solution for galvanic replacement, which reduces gold onto the surface of the Ag NPs and etches the interior to produce hollow GS-NSs.[47] Our previous studies have demonstrated two strategies for tuning the position of the extinction maximum in the resultant GS-NS:[30,31,47] (1) varying the amount of K-gold solution added to a suspension of Ag NPs or (2) varying the amount of $HAuCl_4$ added to the K-gold solution. We employed the latter strategy in the current study. The SEM and transmission electron microscopy (TEM) images in Figures 1c and S1 confirm the successful formation of hollow spherical nanoshells. As determined from DLS measurements using Malvern NanoSight instrumentation and software, the average hydrodynamic diameter of the GS-NSs was 80 ± 20 nm.

SnO_2-, ATO-, and ZTO-Coated Au NPs. The strategy used to prepare tin-oxide-coated (Au@SnO_2) and doped tin-oxide-coated (Au@ATO and Au@ZTO) Au NPs is outlined in Scheme 1 and detailed in the Supporting Information. The Au NPs were coated with a tin oxide shell using an aqueous sodium stannate solution as the precursor, slightly modifying the method used by Oldfield et al.[48] SnO_2 can be easily formed from an aqueous solution of sodium stannate at pH < 11;[15,49,50] notably, crystalline SnO_2 is the most stable phase at pH values under 11.7.[50] The pH can be controlled by adjusting
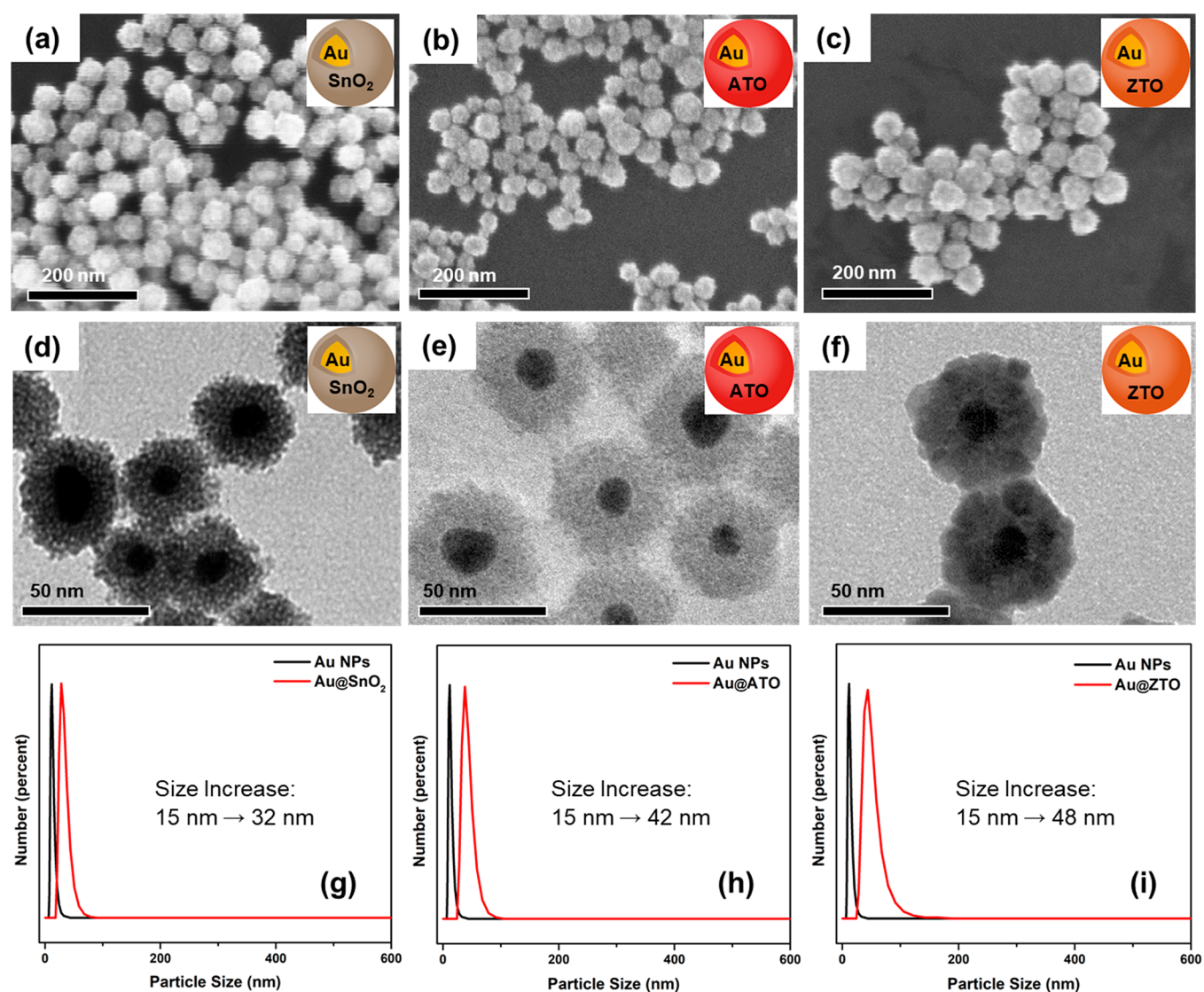
Figure 2. (a−c) SEM images, (d−f) TEM images, and (g−i) hydrodynamic diameter distribution plots for Au@SnO$_2$, Au@ATO, and Au@ZTO nanoparticles, respectively.

the reagent concentration and temperature of the solution.[49] Notably, the pH of the solution decreases with an increase in temperature; consequently, we utilized this principle to form crystallites of SnO$_2$ decorating the Au NP cores. The pH of the sodium stannate solution drops from ∼12.5 to ∼10.5 upon the addition to an Au NP solution at 75 °C. Thus, temperatures above 75 °C were used for 20 min to afford Au NPs coated with undoped tin oxide shells, as demonstrated in Figure 2.

We recently reported the use of a sodium stannate trihydrate precursor coupled with sodium antimonate and sodium zincate precursors, respectively, to generate uniform ATO and ZTO nanoparticles.[15] Recognizing the effectiveness of these precursors in generating doped tin oxide nanoparticles synthesized from sodium stannate, we used in the present study a modification of the original recipe by Oldfield et al.[48] to prepare ATO and ZTO shells on plasmonic nanoparticles. Our methodology started with an aqueous dispersion of Au NPs and separately used sodium antimonate and sodium zincate solutions, respectively, in addition to the sodium stannate solution. After several preliminary trials involving systematic adjustments of the concentrations, we were able to

successfully grow ATO and ZTO shells around the Au NPs with uniformities and thicknesses similar to those found with the undoped SnO$_2$ shells. Sodium antimonate is sparingly soluble in water; consequently, a temperature of ∼90 °C was required to dissolve this precursor and form an aqueous solution, which was then added to the sodium stannate solution maintained at 75 °C in a pressure vessel. The eventual temperature of 150 °C utilized in the recipe ensured complete dissolution of sodium antimonate and subsequent doping of antimony in the tin oxide shell. The zinc precursor was prepared using zinc nitrate and sodium hydroxide, which plausibly led to the formation of an aqueous sodium zincate solution. This solution was then combined with the sodium stannate solution as described above. Doping was confirmed using X-ray diffraction (XRD), X-ray photoelectron spectroscopy (XPS), and TEM−energy-dispersive X-ray spectroscopy (EDX) measurements and is discussed in detail in later sections.

SEM and TEM were used to determine the size and morphology of the nanoparticles. The SEM and TEM images in Figures 2a and 2d, respectively, of the Au@SnO$_2$
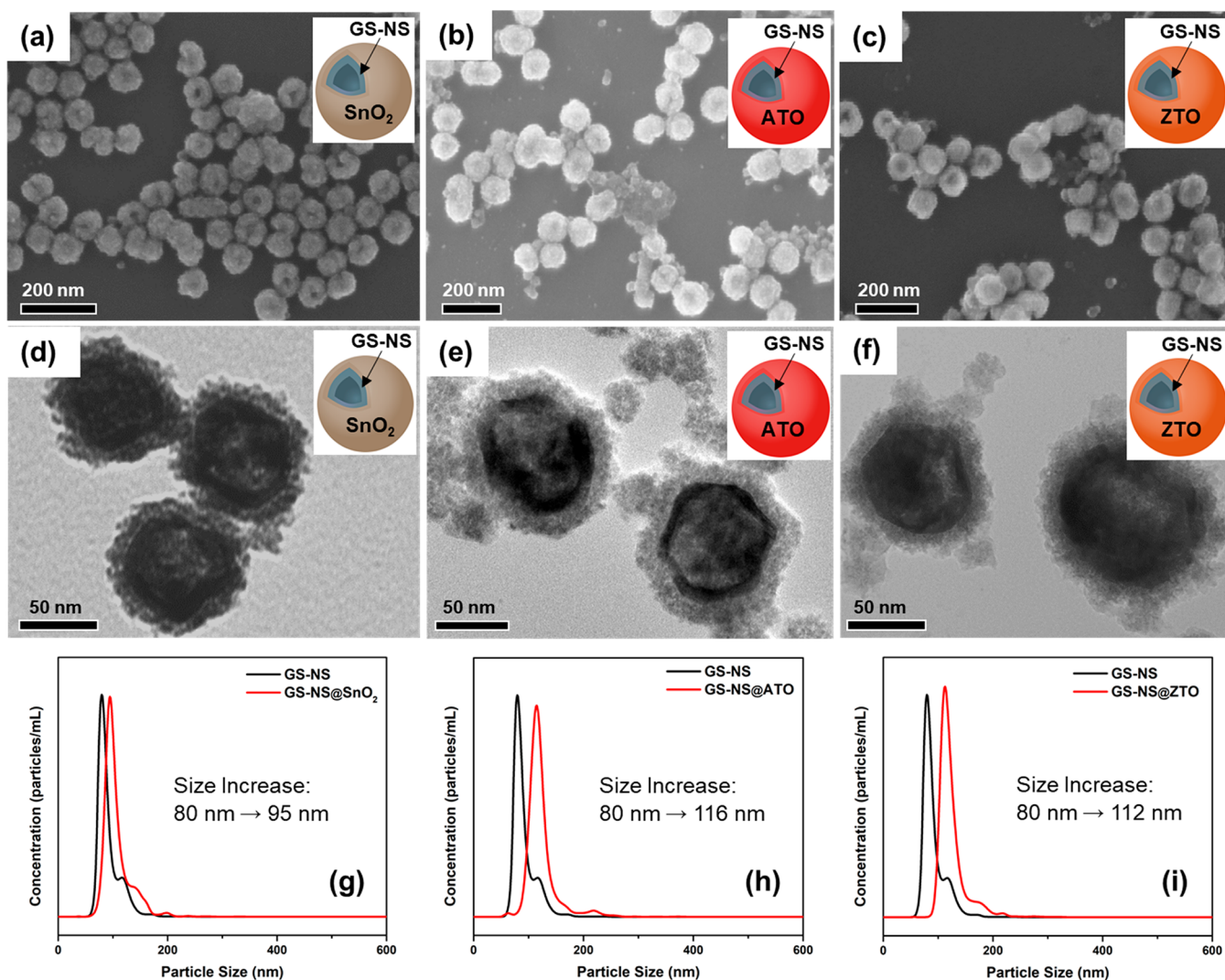
Figure 3. (a−c) SEM images, (d−f) TEM images, and (g−i) hydrodynamic diameter distribution plots of GS-NS@SnO$_2$, GS-NS@ATO, and GS-NS@ZTO nanoparticles, respectively.

nanoparticles show that they are all covered with a uniform tin oxide shell of ~10 nm thickness. The ATO- and ZTO-coated Au NPs exhibited a similar uniform morphology albeit with slightly thicker shells (Figure 2b,c,e,f), making these the first examples of doped metal oxide shells on plasmonic cores. Dynamic light scattering (DLS) measurements were conducted to quantify the size of the particles and the thickness of the tin oxide shells. The DLS data (Figure 2g−i) show that the undoped Au@SnO$_2$ nanoparticles had an average diameter of 32 ± 8 nm. Given that the average hydrodynamic diameter of the Au NPs was 15 ± 5 nm, these measurements indicate that the SnO$_2$ shells have an average thickness of 9 ± 2 nm. The Au@ATO nanoparticles have an average diameter of 42 ± 10 nm, while the Au@ZTO nanoparticles have an average diameter of 48 ± 15 nm; correspondingly, the ATO shells have an average thickness of 14 ± 3 nm, and the ZTO shells have an average thickness of 17 ± 5 nm. The DLS results are consistent with our observations by SEM and TEM.

SnO$_2$-, ATO-, and ZTO-Coated GS-NSs. The synthesis procedure used to coat the SnO$_2$, ATO, and ZTO shells on the GS-NSs was similar to that for the Au NPs with only slight variations as detailed in the Supporting Information. The SEM and TEM images in Figure 3a and 3d, respectively, of the

SnO$_2$-coated GS-NSs show that they are all covered with a thin uniform tin oxide shell having a thickness of ~10−15 nm. This SnO$_2$ coating recipe is highly reproducible. The particles coated with ATO and ZTO also exhibited similar morphologies along with smaller free tin oxide particles, as illustrated in Figure 3b,c,e,f. The number of free tin oxide particles formed can be reduced by lowering the amount of the sodium stannate solution used and/or by judiciously adjusting the concentration of the Au NP and GS-NS solutions used. Provided that all procedures are followed as detailed in the Supporting Information, the formation of free tin oxide nanoparticles can be minimized during the synthesis of GS-NS@ATO and GS-NS@ZTO nanoparticles.

Measurements of the hydrodynamic diameter using Malvern NanoSight (Figure 3g−i) found that, for the coated GS-NSs, the undoped SnO$_2$ shells were about 8 ± 3 nm thick on average, with a total average diameter of 95 ± 25 nm for the coated GS-NS@SnO$_2$ nanoparticles. As in the case of the Au NP cores, vide supra, the ATO and ZTO shells were slightly thicker in comparison to the undoped SnO$_2$ shell. The average diameter of the GS-NS@ATO nanoparticles was 115 ± 28 nm, while the average diameter for the GS-NS@ZTO nanoparticles was found to be 112 ± 25 nm. According to these

measurements, the ATO shells had an average thickness of 18 ± 4 nm in the GS-NS@ATO nanoparticles, and the ZTO shells in the GS-NS@ZTO nanoparticles had an average thickness of 16 ± 3 nm. The DLS measurements from Malvern NanoSight are consistent with the thicknesses observed in the SEM and TEM images.

During the course of the nanoparticle syntheses, we discovered that elevated reaction temperatures led to greater crystallinity of the tin oxide shells. For example, XRD studies on the particles synthesized at 75 °C failed to show observable peaks for SnO_2 and ATO in the XRD patterns; however, upon increasing the temperature to 150 °C, we could readily confirm the presence of SnO_2 and ATO phases by XRD. These studies are discussed in greater detail in the next section. Importantly, we also discovered that the use of metal autoclaves and inadequately cleaned glass pressure vessels led to the coformation of free tin oxide nanoparticle contaminants. In contrast, glass pressure vessels capable of withstanding temperatures of ~150 °C with Teflon caps gave few or no free tin oxide nanoparticle contaminants when the glassware was thoroughly cleaned twice with aqua regia prior to each nanoparticle synthesis. As reported above, the formation of free tin oxide nanoparticles could also be minimized by decreasing the amount of sodium stannate precursor. Interestingly, we also found that decreasing the amount of sodium stannate solution led to slightly decreased shell thicknesses. Overall, the analyses by SEM and TEM showed that the doped tin-oxide-coated core−shell nanoparticles were spherical with monodisperse size distributions (Figures 2 and 3).

ζ-potential measurements were carried out to determine the surface charge and colloidal stability of the nanoparticles. The ζ-potential data in Table S2 reveals that the tin oxide shell increases the surface charge of the nanoparticles and stabilizes them.[51] We have found that the nanoparticles are stable in solution for at least 1 year even in the absence of any surfactant, which opens the door for further surface functionalization and possible applications. This colloidal stability can be attributed to the negative charge on the surface of the tin oxide shells, which is maintained and in some cases increased after doping with antimony and zinc (Table S2). For photoluminescence (PL) measurements, stand-alone SnO_2, ATO, and ZTO nanoparticles were also synthesized according to a previously reported method, where we used water instead of a plasmonic core as the starting solution.[15] As determined by SEM and TEM image analysis, the average diameters of the stand-alone SnO_2, ATO, and ZTO nanoparticles were 31 ± 4, 31 ± 4, and 31 ± 5 nm, respectively (Figure S2).

Crystal Structure of the Nanoparticles. Powder XRD patterns were recorded to identify the crystalline phases present in the nanoparticles (Figure 4). The XRD patterns of the Au@SnO_2 nanoparticles confirm the presence of face-centered-cubic (fcc) gold[38,52] (JCPDS 04-0784), with peaks at 2θ = 38.12°, 44.26°, 64.80°, 77.55°, and 81.60° corresponding to the (111), (200), (220), (311), and (222) crystalline planes, respectively. The XRD patterns for Au@SnO_2 also demonstrate the presence of the tin oxide rutile phase (JCPDS 77-0451),[52] with strong peaks for the (110), (101), and (211) crystalline planes observed at 2θ = 26.52°, 33.89°, and 51.74°, respectively. This tetragonal phase of tin oxide with space group $P4_2/mnm$ (commonly referred to as cassiterite) is the typical structure adopted by tin oxides synthesized from sodium stannate.[50,53] Gold and silver both crystallize into fcc
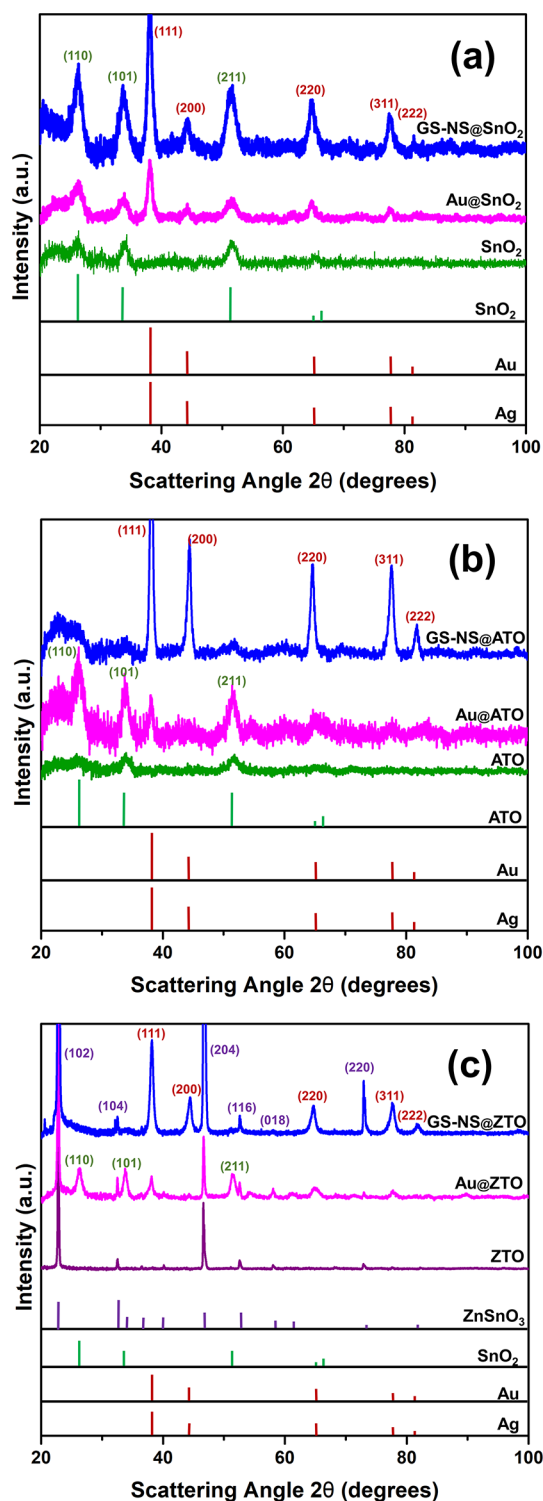

Figure 4. Powder XRD patterns for (a) SnO_2 nanoparticles, Au@SnO_2 and GS-NS@SnO_2, (b) ATO nanoparticles, Au@ATO and GS-NS@ATO, and (c) ZTO nanoparticles, Au@ZTO and GS-NS@ZTO, with their respective reference line patterns. The XRD patterns for the stand-alone SnO_2, ATO, and ZTO nanoparticles were adapted from ref 15. Copyright 2019 American Chemical Society.

structures with similar lattice constants (4.087 and 4.086 Å for Au and Ag, respectively); consequently, it is straightforward to perform a galvanic replacement reaction to obtain their alloy.[54] This phenomenon was consistently observed in all of our samples, where the XRD patterns for the GS-NSs (and their

composite particles) exhibited peaks corresponding to an alloy of gold and silver (JCPDS 04-0784 and 04-0783).[55] For example, the GS-NS@SnO_2 nanoparticles contain fcc cubic phase peaks at 2θ = 38.11°, 44.29°, 64.75°, 77.64°, and 81.60°, which closely resemble the peaks obtained for gold in the Au@SnO_2 nanoparticles. For the GS-NS@SnO_2 nanoparticles, the (110), (101), and (211) crystalline planes of rutile tin oxide were also observed at 2θ = 26.28°, 33.68°, and 51.58°, respectively.

Figure 4 also shows that the XRD peak patterns for the ATO-coated particles are similar to the patterns for the undoped SnO_2-coated particles, which is consistent with the literature for ATO phases (JCPDS 21-1251).[15,27] The (110), (101), and (211) crystalline planes of rutile tin oxide are observed for both Au@ATO and GS-NS@ATO nanoparticles. The peaks corresponding to the (111), (200), (220), and (311) crystalline planes of fcc gold and gold−silver alloy are also observed in the Au@ATO and GS-NS@ATO XRD patterns, respectively.

High-resolution transmission electron microscopy (HRTEM) images were also collected to provide complementary information regarding the various phases and to determine their spatial distribution within the nanoparticles (Figure S3). In the Au@SnO_2 and GS-NS@SnO_2 nanoparticles, the (111) crystalline planes are consistent with fcc gold, with corresponding d spacing of 0.23 and 0.22 nm for each sample, respectively. Lattice planes with d spacing of 0.34 nm are also observed in the HRTEM images, which indicates the presence of the (110) crystalline plane of rutile tin oxide surrounding the Au NP core. This result provides further confirmation of the core−shell morphology of the nanoparticles. The HRTEM images for the GS-NS@SnO_2 nanoparticles also demonstrate this core−shell morphology, with the crystalline planes of gold−silver alloy and rutile tin oxide observed in the core and shell, respectively.

In Figure S4, the HRTEM image of the Au@ATO sample confirms retention of the rutile tin oxide structure after doping with antimony, as indicated by the d spacing along the $[1\bar{1}0]$ zone axis. The HRTEM image shows the characteristic d spacing of 0.31 and 0.37 nm in the surrounding shell corresponding to the (110) and (001) planes of ATO, respectively.[56] This cassiterite structure is commonly observed for antimony-doped tin oxides with <30% doping, as in our case. In the HRTEM image of the GS-NS@ATO nanoparticles in Figure S5, one can observe the characteristic d spacing of 0.22 and 0.30 nm along the [010] zone axis, corresponding to the (111) and $(\bar{1}10)$ planes of ATO, respectively.

The HRTEM images in Figures S3−S5 also confirm the polycrystalline nature of the SnO_2 and ATO shells grown on both the Au NP and GS-NS cores, consistent with the XRD measurements. For gas-sensing applications, the sensitivity increases with decreasing grain size until 6 nm, which is double the thickness of the space-charge layer in tin oxide.[39,40] A common challenge with gas-sensor device fabrication is controlling the grain growth.[38,39] The advantage of the sodium stannate method is that it yields tin oxide with grain sizes of ∼6−7 nm.[15] As calculated in Table S3, the SnO_2 shells in our case have a grain size of 6 and 10 nm in the Au@SnO_2 and GS-NS@SnO_2 nanoparticles, respectively. Even upon doping with antimony, small grain sizes are retained at 9 and 6 nm for the Au@ATO and GS-NS@ATO nanoparticles, respectively. Importantly, the grain-dependent conduction and porosity of the doped tin oxide core−shell materials prepared here make

them promising nanomaterials for gas sensing at ambient temperatures.

In contrast to the ATO-coated nanoparticles, the XRD patterns in Figure 4 of the ZTO-coated nanoparticles showed the presence of a $ZnSnO_3$ phase (JCPDS 11-0274),[57] indicating that the crystal structure of tin oxide changes upon doping with zinc, in accordance with previous literature.[57] Specifically for the Au@ZTO nanoparticles, peaks arising from a $ZnSnO_3$ phase at 2θ = 22.80°, 32.52°, 38.11°, 46.64°, 52.59°, 58.09°, and 72.93° corresponding to the (102), (104), (204), (116), (018), and (220) planes, respectively, are observed in addition to rutile tin oxide peaks at 2θ = 26.38°, 33.87°, and 51.45° corresponding to the (110), (101), and (211) planes, respectively.[58] Separately for the GS-NS@ZTO nanoparticles, the XRD pattern in Figure 4 shows exclusively the $ZnSnO_3$ phase, with no observable rutile tin oxide peaks. This observation is consistent with the HRTEM images in Figures S6 and S7 for the ZTO-coated nanoparticles (vide infra).

In complementary studies, the HRTEM images in Figures S6 and S7 confirm the presence of a $ZnSnO_3$ phase in the ZTO shells. The HRTEM image in Figure S6 for the Au@ZTO nanoparticles shows characteristic d spacing of 0.29, 0.38, and 0.58 nm along the $[0\bar{1}0]$ zone axis, corresponding to the (104), (102), and $(\bar{1}00)$ planes of the $ZnSnO_3$ phase, respectively. Similarly, the HRTEM image in Figure S7 for the GS-NS@ZTO nanoparticles along the $[0\bar{1}0]$ zone axis reveals characteristic d spacing of 0.23, 0.24, and 0.38 nm in the surrounding shell corresponding to the $(2\bar{1}3)$, (006), and $(10\bar{2})$ planes of the $ZnSnO_3$ phase, respectively. Interestingly, HRTEM imaging also reveals larger crystallites in the ZTO shells compared to those in the ATO shells, which corroborates the XRD observations. A more crystalline $ZnSnO_3$ phase in ZTO compared to both the SnO_2 and ATO phases obtained using the sodium stannate method is consistent with the crystallinities of the stand-alone single-component nanoparticles.[15] As calculated from the XRD data (Table S3), the ZTO phases have an average grain size of 40 and 56 nm in the Au@ZTO and GS-NS@ZTO nanoparticles, respectively. These values are higher than those expected from the measured shell thicknesses; it is possible, however, that the calculated values were skewed because of the presence of small amounts of highly crystalline stand-alone $ZnSnO_3$ impurities. The $(\bar{1}10)$, (101), and (011) planes, corresponding to d spacing of 0.29, 0.28, and 0.28 nm, respectively (characteristic of fcc gold), are also observed within the core of the Au@ZTO nanoparticles as expected (Figure S8).[59] The HRTEM images in Figures S6 and S8 indicate that larger crystallites corresponding to $ZnSnO_3$ appear to occupy the outer half of the shell, while the area immediately surrounding the gold core is occupied by smaller crystallites of rutile tin oxide. Interestingly, the rutile tin oxide peaks in Au@ZTO have a corresponding crystallite size of 14 nm, which is the largest observed for the rutile phase among all of the samples.

Elemental Composition of the Nanoparticles. We subjected the samples to analysis by XPS to determine the doping percentage in the tin oxide shells (Figure 5 and Table 1). The XPS spectrum in Figure 5 shows the Sn $3d_{5/2}$ and Sn $3d_{3/2}$ peaks at 486.0 and 494.5 eV, respectively, indicating the presence of tin oxide in all of the samples (Figure 5a,b). The oxygen peaks around 530.0 eV observed in Figure S9 are consistent with the presence of a metal oxide, which would be tin oxide in the present study. For the ATO-coated

Table 1. XPS-Derived Relative Atomic Concentrations of Silver, Gold, Tin, Oxygen, Zinc, and Antimony in the Various Tin-Oxide-Coated Samples

sample	relative atomic concentration (%)					
	Ag 3d	Au 4f	Sn $3d_{5/2}$	O 1s	Zn $2p_{3/2}$	Sb $3d_{5/2}$
Au@SnO$_2$		2	14	84		
Au@ATO		1	16	82		1
Au@ZTO		1	17	78	5	
GS-NS@SnO$_2$	2	1	17	80		
GS-NS@ATO	1	1	23	73		3
GS-NS@ZTO	3	1	15	79	2	

nanoparticles, the Sb $3d_{5/2}$ peak overlaps with the O 1s peak. However, the Sb $3d_{3/2}$ peak is prominent, which conclusively demonstrates the presence of antimony in the outer-shell structure (Figure 5c). Direct quantitative analysis of the Sb $3d_{5/2}$ peak was complicated because of its overlap with the O 1s peak. However, using the Sb $3d_{5/2}$/Sb $3d_{3/2}$ peak ratio as ~1.5 for antimony,[60] we focused on the Sb $3d_{3/2}$ peak and calculated the intensity of the Sb $3d_{5/2}$ peak according to this ratio. Quantitative analysis revealed that antimony doping with respect to tin in the tin oxide lattice was 8% and 12% for the Au@ATO and GS-NS@ATO particles, respectively (Table 1), which is a doping percentage similar to those for commercially available ATO nanomaterials.[61]

For the ZTO-coated nanoparticles, the XPS spectrum showed a Zn $2p_{3/2}$ peak at 1021.0 eV, consistent with the presence of Zn^{2+} in the structure (Figure 5d). As reported previously,[62] ZTO structures with a zinc doping percentage of ~10–12% exhibit the lowest resistivity and highest carrier concentration; consequently, our goal was to generate ZTO-coated nanoparticles with this doping percentage. Notably, in our Au@ZTO and GS-NS@ZTO nanoparticles, the ZTO shells had zinc doping percentages of 23% and 9%, respectively (see Table 1). For the Au@ZTO nanoparticles, the zinc doping percentage as measured by XPS is higher than targeted, which is plausibly due to the concentration of zinc in the outer-phase ZnSnO$_3$ regions of the shell, as noted above regarding

the HRTEM studies (see also Figure S6). In our hands, these doping percentages tend to vary from batch to batch by about ±2% for the various ATO- and ZTO-coated nanoparticles. We note also that the intensities of the gold (Au 4f) and silver (Ag 3d) signals were weak in the XPS spectra, and the corresponding atomic concentrations for Au and Ag were low for the coated particles, indicating that these elements were encapsulated within the tin oxide shells. Compared to the nanoparticles having undoped shells, the XPS-derived atomic percentages of gold and silver appear to be marginally lower for the nanoparticles having ATO and ZTO shells on both the Au NP and GS-NS cores. This observation is consistent with SEM/TEM imaging and size measurements, wherein the ATO and ZTO shells are thicker than the undoped SnO$_2$ shells. Importantly, the percentages of antimony and zinc can be tuned by varying the amounts of sodium antimonate and sodium zincate, respectively, used during the syntheses.

To provide complementary elemental composition data as well as information regarding the distribution of the various elements within the nanoparticles, we subjected the samples to analysis by TEM−EDX and scanning TEM (STEM) elemental mapping. The semiquantitative atomic concentrations obtained from TEM−EDX measurements are listed in Table 2.

Table 2. EDX-Derived Relative Atomic Concentrations of Silver, Gold, Tin, Oxygen, Zinc, and Antimony in the Various Tin-Oxide-Coated Samples

sample	relative atomic concentration (%)					
	Ag	Au	Sn	O	Zn	Sb
Au@SnO$_2$		6	25	69		
Au@ATO		3	20	77		2
Au@ZTO		7	19	71	3	
GS-NS@SnO$_2$	6	6	14	75		
GS-NS@ATO	8	4	13	73		2
GS-NS@ZTO	8	6	10	75	1	

Compared to the XPS analyses, which probe only the interfacial regions of the nanoparticles, the atomic concen-
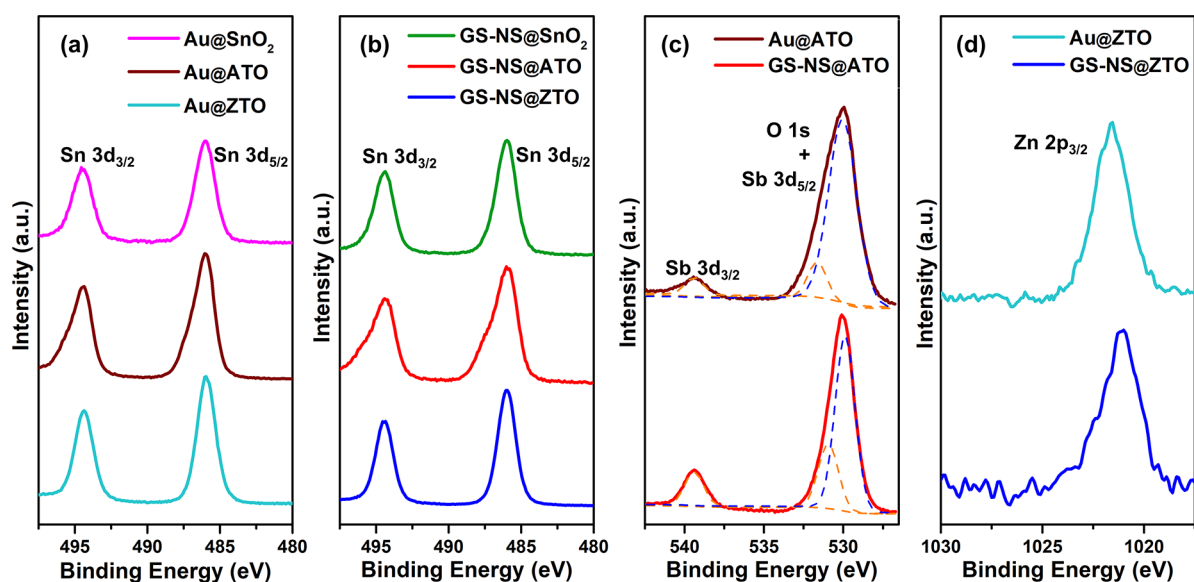
Figure 5. XPS spectra for the (a) Sn 3d region for all coated Au nanoparticles, (b) Sn 3d region spectra for all coated GS-NSs, (c) Sb 3d region for ATO-coated samples, and (d) Zn 2p region for ZTO-coated samples.

trations of gold and silver are much higher in the EDX measurements, which probe the bulk nanoparticle composition. This comparison provides further support that the Au NP and GS-NS cores lie within the tin oxide shells. We also conducted STEM−EDX line spectra of the respective elements to provide additional confirmation of the core−shell morphology (Figures S10 and S11). Because the oxygen signal is significantly stronger than most of the other elements, the distribution of oxygen is omitted from all of the STEM line spectra for the purpose of clarity. The distribution of tin in the Au@SnO$_2$ and GS-NS@SnO$_2$ nanoparticles extends well beyond the distribution of gold and silver in their respective nanoparticles, confirming the presence of tin in the nanoparticle shells.

TEM−EDX measurements and STEM mapping were further conducted on the antimony- and zinc-doped samples. As calculated in Table 2, the antimony doping percentage was found to be 7% and 13% in the Au@ATO and GS-NS@ATO nanoparticles, respectively. Given that the XRD patterns for the undoped and antimony-doped tin oxide were quite similar (vide supra), we performed STEM mapping to determine the antimony distribution throughout the tin oxide lattice. As illustrated in Figures 6a and S15, gold and silver were confined only to the inner regions of the nanoparticle. Tin and oxygen distributions extend out wider to cover more of the nanoparticle volume, consistent with encapsulation of the inner gold and gold−silver cores within a tin oxide shell in the respective nanoparticles. The STEM mapping images of the Au@ATO and GS-NS@ATO nanoparticles in Figures 6a and

S15 further show that the antimony distribution closely resembles the distribution of tin and oxygen. The STEM line spectra of Au@ATO and GS-NS@ATO in Figures S12 and S13 also show that the tin and antimony distributions extend wider than the gold and silver distributions in their respective nanoparticles, which is consistent with an antimony-doped tin oxide shell. In combination with the XRD pattern, HRTEM imaging, and STEM line spectra and mapping, we can conclude that antimony is doped into the tin oxide lattice because only the tin oxide, gold, and silver phases are present and no other antimony species are observed.

STEM mapping of the Au@ZTO and GS-NS@ZTO nanoparticles was also conducted to determine the distribution of zinc with respect to tin in the surrounding shells (Figures 6b and S17). The distribution of zinc was found to be largely uniform throughout the structure, as is evident from the EDX map. Both the tin and zinc distributions mimic each other and extend beyond the gold and silver regions, confirming that the shell is comprised of these two species. This trend was also observed in the line spectra for these nanoparticles (Figures S14 and S15, respectively). As per the EDX results in Table 2, the zinc doping percentages were found to be 14% and 9% for the Au@ZTO and GS-NS@ZTO nanoparticles, respectively. The relative concentrations of the antimony and zinc dopants with respect to tin remain roughly the same in both XPS and EDX measurements, while the relative concentrations of gold and silver with respect to tin are much higher in EDX measurements compared to XPS, which provides further confirmation that the dopants are incorporated within the tin oxide shells surrounding the metal cores.

Optical and Electrical Properties. We previously described the optical properties of the SnO$_2$, ATO, and ZTO nanoparticles synthesized using a sodium stannate method.[15] Diffuse-reflectance spectroscopy measurements recorded the optical band gap of the SnO$_2$ nanoparticles at 3.89 eV. The band gap was reduced upon doping with both antimony and zinc. The ATO nanoparticles had a reduced band gap of 3.66 eV, while the ZTO nanoparticles had a more modest reduced band gap of 3.85 eV.[15] The ATO nanoparticles showed much stronger absorption in the visible region, with the absorption extending to ∼700 nm. However, greater utilization of the visible and near-IR (NIR) regions of the solar spectrum is needed to render these doped tin oxide materials more broadly effective for photocatalytic and optoelectronic applications.

We used UV−vis spectroscopy to measure the optical extinctions of the core−shell nanoparticles (Figure 7). Au NPs and GS-NSs exhibit strong activity in the visible and NIR regions because of their LSPRs.[47] LSPR is a unique property exhibited by metal nanoparticles and nanoshells wherein the collective oscillation of surface electrons couples with incident light of the same frequency, leading to extinctions that extend to visible and even NIR wavelengths.[47] As shown in Figure 7, the Au NPs exhibited an LSPR extinction maximum at ∼520 nm, which is appropriate for their measured size.[21,47] When coated with tin oxide (both doped and undoped), the LSPR peak red-shifted by ∼20−40 nm. This red shift is consistent with previous observations of high-refractive-index coating materials on metal nanoparticles; notably, the refractive index of SnO$_2$ (∼2.006) is greater than that of water (∼1.333).[48]

The extinction spectra of GS-NSs are presented in Figure 8 before and after coating with the three types of tin oxide shells. The advantage of using GS-NSs, as we demonstrate herein, is
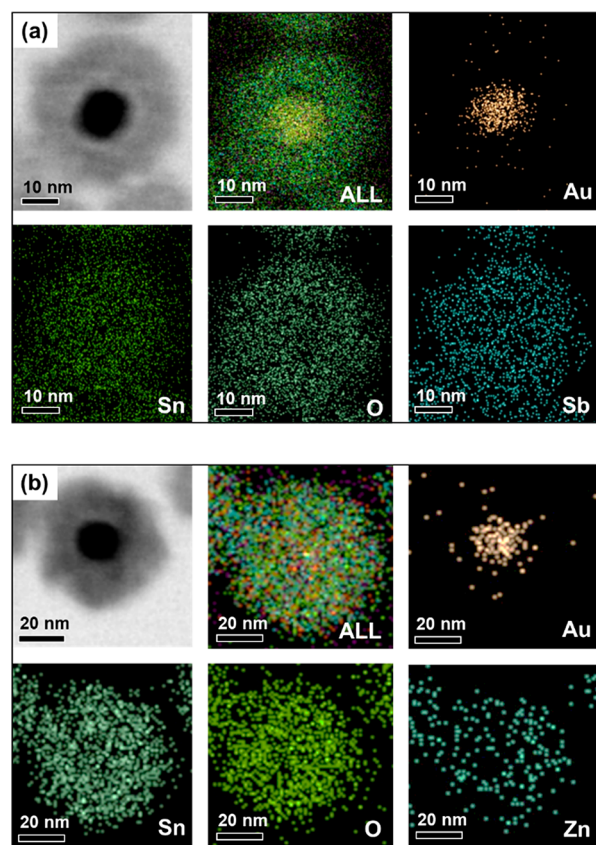

Figure 6. STEM images and elemental mapping of the (a) Au@ATO and (b) Au@ZTO nanoparticles, showing the distribution of constituent elements in the nanoparticles.
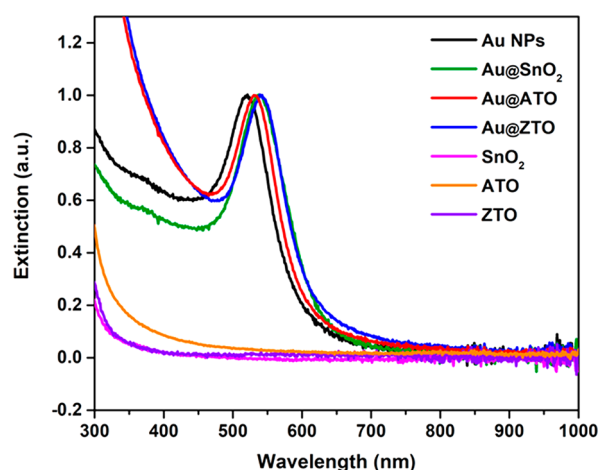
Figure 7. Extinction spectra of Au NPs before and after coating with SnO$_2$, ATO, and ZTO shells. The extinction spectra of stand-alone SnO$_2$, ATO, and ZTO nanoparticles are included for comparison.

that the surface plasmon resonance bands can be tuned. We synthesized three different types of GS-NSs with LSPR extinction bands centered at ~680, ~750, and ~840 nm. The SPR wavelength was adjusted by varying the amount of HAuCl$_4$ in the K-gold solution and also by adjusting the reaction time for the galvanic replacement step.[31] Higher concentrations of gold precursor and longer reaction times during the galvanic replacement led to thinner nanoshells, with a higher Au/Ag compositional ratio resulting in higher LSPR extinction wavelengths. Specifically, for the typical concentrations of Ag NPs reported in this paper, ~1, ~1.5, and ~2 mL of a 1% HAuCl$_4$ solution were added to 100 mL of a K$_2$CO$_3$ solution, and then 10 mL of Ag NPs was added to obtain GS-NSs with extinction maxima at ~680, ~750, and ~840 nm, respectively. The broad extinction of GS-NSs in the visible and NIR regions coupled with the tunability of the extinction is an advantageous feature that renders their utilization attractive. Effectively, we can shift the extinction maximum from ~500 nm to near and perhaps beyond the 1000 nm mark, enabling wider utilization of the solar spectrum by the various tin oxide materials. Similar to the Au NPs, a red shift upon coating with tin oxide was also apparent in the GS-NSs, which can be attributed to the surrounding dielectric as described above. Thus, for gas-sensing applications, the presence of the Au NP and GS-NS cores can enhance the sensing properties of doped tin oxide nanomaterials.[43]
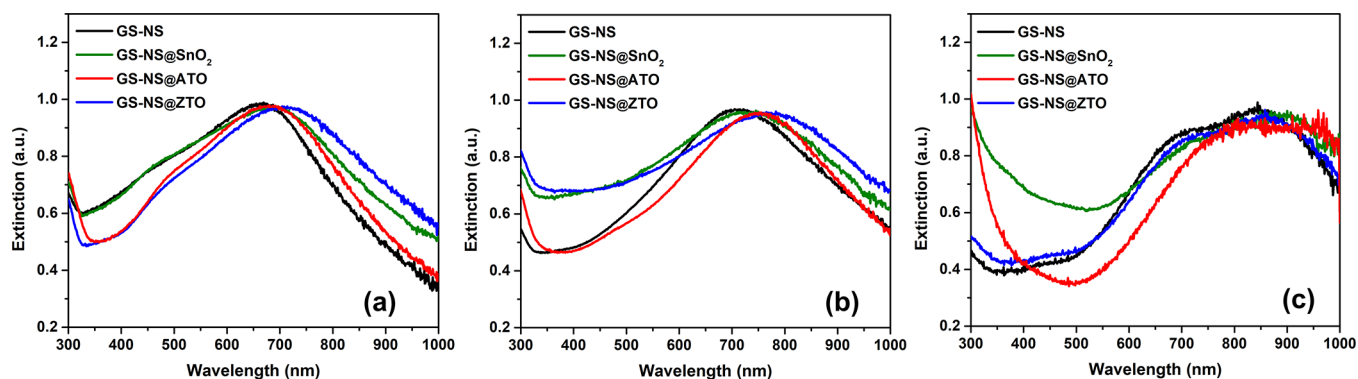
Many applications that utilize metal oxide nanoparticles suffer from limitations due to electron−hole recombination.[4,32] In these cases, electron and hole pairs generated from the absorption of light readily recombine, rendering them unavailable for utilization in the targeted photocatalytic application.[32] Many strategies, including doping and the use of plasmonic nanostructures, have been pursued in an effort to minimize the rate of electron−hole recombination in semiconductor catalysts.[4,64] For nanoparticle catalysts, as discussed earlier, the metal oxides are most commonly used as core nanoparticles in conjunction with adjacent and/or coated plasmonic materials. For example, Au NPs have been used to decorate the outside of a metal oxide photocatalytic core to quench its rate of electron−hole recombination, especially in the case of photocatalysts based on TiO$_2$ and SnO$_2$ nanoparticles.[29,33,63] Furthermore, previous studies conducted by our group using gold-decorated TiO$_2$ nanoparticles demonstrated the effective suppression of electron−hole recombination, leading to enhanced photocatalytic activity.[29] Studies conducted by Khan et al. found that photoelectrodes comprised of tin oxide nanoparticles exhibited higher anodic and cathodic currents under visible-light irradiation when decorated with gold.[33] Also, the gold-decorated tin oxide nanoparticles showed an approximately 4-fold increase in the photocatalytic activity. These enhancements can plausibly be correlated with their observation that gold decoration significantly suppressed electron−hole recombination in the tin oxide nanoparticles.

In contrast to previous studies, we employ in the present study a core−shell nanoparticle architecture in which the plasmonic component is the core, while the tin oxide material is the shell. We conducted PL studies to examine the possibility of plasmonic quenching of electron−hole recombination in our tin-oxide-based nanomaterials. The PL intensity in metal oxides arises from the energy emitted by electrons that relax and recombine with holes; consequently, a decrease in the PL intensity corresponds to a decrease in the rate of electron−hole recombination.[33] We used an excitation wavelength of 315 nm to perform the PL measurements for all samples (Figure 9). For a meaningful comparison, the PL intensities were normalized with respect to the particle concentration and volume of the tin oxide material per particle. Importantly, Figure 9b shows that when the PL intensities were normalized with respect to the volume of the tin oxide material per particle, nearly complete suppression of electron−hole recombination occurred. This remarkably

Figure 8. Extinction spectra of GS-NSs with changes in the absorption maximum (λ_{max}) before and after coating with SnO$_2$, ATO, and ZTO shells. The tin oxide shells were coated onto GS-NSs with initial λ_{max} values at (a) ~680, (b) ~750, and (c) ~840 nm, respectively.
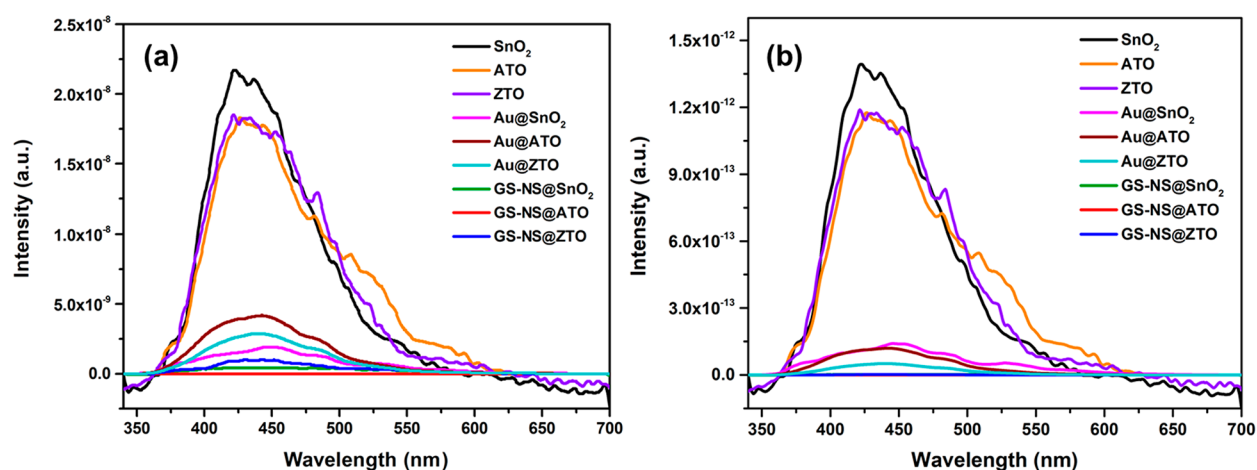
Figure 9. PL spectra of the SnO$_2$, ATO, ZTO, Au@SnO$_2$, Au@ATO, Au@ZTO, GS-NS@SnO$_2$, GS-NS@ATO, and GS-NS@ZTO nanoparticles normalized with respect to the (a) particle concentration and (b) particle concentration + volume of the tin oxide material per particle. An excitation wavelength of 315 nm was used to generate the spectra. The PL spectra for the stand-alone SnO$_2$, ATO, and ZTO nanoparticles were adapted from ref 15. Copyright 2019 American Chemical Society.

effective suppression demonstrates a strikingly important advantage of having a plasmonic particle as the core and a metal oxide as the shell.

We conducted additional PL measurements using an excitation wavelength of 200 nm, which is well above the band gap;[15] notably, a similar quenching of electron−hole recombination was observed (Figure S18). Furthermore, Figures 9b and S18b indicate that the suppression of electron−hole recombination per volume of tin oxide appears to be more effective with a GS-NS core than with a Au NP core. Hollow nanostructures hold charges better than solid nanoparticles, which is perhaps the reason why recombination is more strongly suppressed by the GS-NS core.[64] Notably, the same trends are observed at both excitation wavelengths. Overall, the plasmonic nanoparticle core−tin oxide shell nanoparticle architectures reported here provide an extraordinarily effective suppression of electron−hole recombination, further emphasizing the potential importance of this design, with the tunable plasmonic GS-NS cores offering perhaps the greatest utility.

Photocurrent generation stands as an another important application for solar-activated metal oxides, and many researchers have explored various doping strategies to enhance the efficiency of such systems.[65−67] Doping can extend the range of light absorption of metal oxides to the visible region via band-gap narrowing and/or via additional absorption peaks in the 400−800 nm range. In addition, doping can increase the conductivity of metal oxides by injecting additional electrons into the conduction band. Both of these strategies can enhance the photocurrent generation of metal oxides such as TiO$_2$, ZnO, and perovskites.[65−67] Even though plasmonic enhancement using light at the visible and NIR regions is an import field of investigation, few previous photocurrent generation studies have explored the use of plasmonic activation combined with metal oxide doping. As demonstrated herein, the near-complete suppression of electron−hole recombination by the plasmonic core offers enhanced utility for the generated charge carriers. Widely used TiO$_2$ and ZnO have multiple close-lying levels in the conduction band, which can lead to intraband transitions and diminished electron mobilities.[68,69] For high conductivities upon heavy doping, a single dispersive level in the conduction band, like that in SnO$_2$, is preferred because of the small carrier mass at the conduction band and, consequently, more effective transport of the photogenerated electrons.[68] In the present report, we combine the two phenomena of doping for conductivity and LSPR for light absorption in the same nanoparticle design, along with the careful choice of the metal oxide. As discussed earlier, ~10% antimony doping in tin oxide can remarkably enhance the conductivity of tin oxide, quite similar to how tin doping increases the conductivity of indium oxide as ITO.[68,70] When this high conductivity is coupled with the strong LSPR-induced absorption of light in the visible and NIR regions from the plasmonic Au NP and GS-NS cores, these composite doped tin oxide core−shell nanoparticles stand as promising materials for photocurrent generation.

■ CONCLUSIONS

We synthesized Au NPs and GS-NSs as core plasmonic particles and coated them with uniform tin oxide and antimony- and zinc-doped tin oxide shells. The uniformity of the metal oxide shells was maintained after doping, even in the absence of surfactant. Furthermore, the absence of surfactant molecules or plasmonic seeds covering the metal oxide surface offers an increase in the effective surface area and thus enhanced capacity for sensing and photocatalytic applications compared to alternative plasmonic−metal oxide nanoarchitectures. Measurements of the optical properties showed that the SnO$_2$-coated plasmonic nanoparticles exhibited strong extinctions in the visible and NIR regions; moreover, the position of the extinction maximum was selectively tuned within this region. Importantly, the incorporation of Au NP and GS-NS cores completely suppressed electron−hole recombination in various tin oxide shell materials, demonstrating a major advantage of the metal oxide-coated plasmonic core architecture. Overall, the combination of tunable doping, strong light absorption across a broad range of wavelengths, and suppression of charge recombination offers a new class of nanomaterials for gas-sensing, optoelectronic, photovoltaic, and photocatalytic applications.

ASSOCIATED CONTENT

Supporting Information

The Supporting Information is available free of charge at https://pubs.acs.org/doi/10.1021/acsanm.0c01702.

Details of the experimental procedures, materials used, and characterization methods; HRTEM images for all nanoparticles; STEM−EDX line spectra for the nanoparticles; ζ potential and crystallite size data for all nanoparticles; additional SEM images of SnO_2, ATO, and ZTO nanoparticles; STEM−EDX elemental mapping images for GS-NS@ATO and GS-NS@ZTO nanoparticles; and additional PL data (PDF)

AUTHOR INFORMATION

Corresponding Author

T. Randall Lee − Department of Chemistry and the Texas Center for Superconductivity, University of Houston, Houston, Texas 77204-5003, United States; orcid.org/0000-0001-9584-8861; Email: trlee@uh.edu

Authors

Riddhiman Medhi − Department of Chemistry and the Texas Center for Superconductivity, University of Houston, Houston, Texas 77204-5003, United States; orcid.org/0000-0002-2368-2468

Chien-Hung Li − Department of Medicinal and Applied Chemistry, Kaohsiung Medical University, Kaohsiung 80708, Taiwan; orcid.org/0000-0003-1643-8368

Sang Ho Lee − Department of Chemistry and the Texas Center for Superconductivity, University of Houston, Houston, Texas 77204-5003, United States

Pannaree Srinoi − Department of Chemistry and the Texas Center for Superconductivity, University of Houston, Houston, Texas 77204-5003, United States

Maria D. Marquez − Department of Chemistry and the Texas Center for Superconductivity, University of Houston, Houston, Texas 77204-5003, United States

Francisco Robles-Hernandez − College of Engineering Technology, University of Houston, Houston, Texas 77204-5003, United States; orcid.org/0000-0001-5587-0802

Allan J. Jacobson − Department of Chemistry and the Texas Center for Superconductivity, University of Houston, Houston, Texas 77204-5003, United States; orcid.org/0000-0002-6540-8846

Tai-Chou Lee − Department of Chemical and Materials Engineering, National Central University, Jhongli City 32001, Taiwan; orcid.org/0000-0002-1695-1201

Complete contact information is available at:
https://pubs.acs.org/10.1021/acsanm.0c01702

Notes

A provisional patent application has been filed (U.S. Patent Application No. 62/799,432).
The authors declare no competing financial interest.

ACKNOWLEDGMENTS

REFERENCES

(1) Yu, X.; Marks, T. J.; Facchetti, A. Metal Oxides for Optoelectronic Applications. *Nat. Mater.* **2016**, *15*, 383.

(2) Raghunath, A.; Perumal, E. Metal Oxide Nanoparticles as Antimicrobial Agents: A Promise for the Future. *Int. J. Antimicrob. Agents* **2017**, *49*, 137−152.

(3) Daghrir, R.; Drogui, P.; Robert, D. Modified TiO_2 For Environmental Photocatalytic Applications: A Review. *Ind. Eng. Chem. Res.* **2013**, *52*, 3581−3599.

(4) Ray, C.; Pal, T. Recent Advances of Metal−Metal Oxide Nanocomposites and their Tailored Nanostructures in Numerous Catalytic Applications. *J. Mater. Chem. A* **2017**, *5*, 9465−9487.

(5) Dey, A. Semiconductor Metal Oxide Gas Sensors: A Review. *Mater. Sci. Eng., B* **2018**, *229*, 206−217.

(6) Ganguly, A.; Anjaneyulu, O.; Ojha, K.; Ganguli, A. K. Oxide-Based Nanostructures for Photocatalytic and Electrocatalytic Applications. *CrystEngComm* **2015**, *17*, 8978−9001.

(7) Liu, Y.; Wang, W.; Xu, X.; Marcel Veder, J.-P.; Shao, Z. Recent Advances in Anion-Doped Metal Oxides for Catalytic Applications. *J. Mater. Chem. A* **2019**, *7*, 7280−7300.

(8) Lu, Y.-H.; Lin, W.-H.; Yang, C.-Y.; Chiu, Y.-H.; Pu, Y.-C.; Lee, M.-H.; Tseng, Y.-C.; Hsu, Y.-J. A Facile Green Antisolvent Approach to Cu^{2+}−Doped ZnO Nanocrystals with Visible-Light-Responsive Photoactivities. *Nanoscale* **2014**, *6*, 8796−8803.

(9) Walukiewicz, W. Defect Formation and Diffusion in Heavily Doped Semiconductors. *Phys. Rev. B: Condens. Matter Mater. Phys.* **1994**, *50*, 5221−5225.

(10) Du, J.; Chen, X.-L.; Liu, C.-C.; Ni, J.; Hou, G.-F.; Zhao, Y.; Zhang, X.-D. Highly Transparent and Conductive Indium Tin Oxide Thin Films for Solar Cells Grown by Reactive Thermal Evaporation at Low Temperature. *Appl. Phys. A: Mater. Sci. Process.* **2014**, *117*, 815−822.

(11) García-Mota, M.; Vojvodic, A.; Abild-Pedersen, F.; Nørskov, J. K. Electronic Origin of the Surface Reactivity of Transition-Metal-Doped $TiO_2(110)$. *J. Phys. Chem. C* **2013**, *117*, 460−465.

(12) Baer, D. R.; Engelhard, M. H.; Johnson, G. E.; Laskin, J.; Lai, J.; Mueller, K.; Munusamy, P.; Thevuthasan, S.; Wang, H.; Washton, N.; Elder, A.; Baisch, B. L.; Karakoti, A.; Kuchibhatla, S. V. N. T.; Moon, D. Surface Characterization of Nanomaterials and Nanoparticles: Important Needs and Challenging Opportunities. *J. Vac. Sci. Technol., A* **2013**, *31*, 050820.

(13) Staller, C. M.; Robinson, Z. L.; Agrawal, A.; Gibbs, S. L.; Greenberg, B. L.; Lounis, S. D.; Kortshagen, U. R.; Milliron, D. J. Tuning Nanocrystal Surface Depletion by Controlling Dopant Distribution as a Route Toward Enhanced Film Conductivity. *Nano Lett.* **2018**, *18*, 2870−2878.

(14) Medhi, R.; Marquez, M. D.; Lee, T. R. Visible-Light-Active Doped Metal Oxide Nanoparticles: A Review of their Synthesis, Properties, and Applications. *ACS Appl. Nano Mater.* **2020**, *3*, 6156−6185.

(15) Medhi, R.; Li, C.-H.; Lee, S. H.; Marquez, M. D.; Jacobson, A. J.; Lee, T.-C.; Lee, T. R. Uniformly Spherical and Monodisperse Antimony- and Zinc-Doped Tin Oxide Nanoparticles for Optical and Electronic Applications. *ACS Appl. Nano Mater.* **2019**, *2*, 6554−6564.

(16) Mi, Y.; Odaka, H.; Iwata, S. Electronic Structures and Optical Properties of ZnO, SnO_2 and In_2O_3. *Jpn. J. Appl. Phys.* **1999**, *38*, 3453.

(17) Harrison, P. G.; Willett, M. J. The Mechanism of Operation of Tin(IV) Oxide Carbon Monoxide Sensors. *Nature* **1988**, *332*, 337.

(18) Tennakone, K.; Bandara, J.; Bandaranayake, P. K. M.; Kumara, G. R. A.; Konno, A. Enhanced Efficiency of a Dye-Sensitized Solar Cell Made from MgO-Coated Nanocrystalline SnO_2. *Jpn. J. Appl. Phys.* **2001**, *40*, L732.

(19) Arnold, M. S.; Avouris, P.; Pan, Z. W.; Wang, Z. L. Field-Effect Transistors Based on Single Semiconducting Oxide Nanobelts. *J. Phys. Chem. B* **2003**, *107*, 659−663.

(20) Yu, S.; Li, L.; Xu, D.; Dong, H.; Jin, Y. Characterization of $SnO_2/Cu/SnO_2$ Multilayers for High Performance Transparent Conducting Electrodes. *Thin Solid Films* **2014**, *562*, 501−505.

(21) Lee, S. H.; Rusakova, I.; Hoffman, D. M.; Jacobson, A. J.; Lee, T. R. Monodisperse SnO$_2$-Coated Gold Nanoparticles Are Markedly More Stable than Analogous SiO$_2$-Coated Gold Nanoparticles. *ACS Appl. Mater. Interfaces* **2013**, *5*, 2479−2484.

(22) Senthilkumar, V.; Senthil, K.; Vickraman, P. Microstructural, Electrical and Optical Properties of Indium Tin Oxide (ITO) Nanoparticles Synthesized by Co-Precipitation Method. *Mater. Res. Bull.* **2012**, *47*, 1051−1056.

(23) Banyamin, Y. Z.; Kelly, J. P.; West, G.; Boardman, J. Electrical and Optical Properties of Fluorine Doped Tin Oxide Thin Films Prepared by Magnetron Sputtering. *Coatings* **2014**, *4*, 732−746.

(24) Huang, Y.; Li, G.; Feng, J.; Zhang, Q. Investigation on Structural, Electrical and Optical Properties of Tungsten-Doped tin Oxide Thin Films. *Thin Solid Films* **2010**, *518*, 1892−1896.

(25) Jain, G.; Kumar, R. Electrical and Optical Properties of Tin Oxide and Antimony Doped Tin Oxide Films. *Opt. Mater.* **2004**, *26*, 27−31.

(26) Bhat, J. S.; Maddani, K. I.; Karguppikar, A. M. Influence of Zn doping on Electrical and Optical Properties of Multilayered Tin Oxide Thin Films. *Bull. Mater. Sci.* **2006**, *29*, 331−337.

(27) Koebel, M. M.; Nadargi, D. Y.; Jimenez-Cadena, G.; Romanyuk, Y. E. Transparent, Conducting ATO Thin Films by Epoxide-Initiated Sol−Gel Chemistry: A Highly Versatile Route to Mixed-Metal Oxide Films. *ACS Appl. Mater. Interfaces* **2012**, *4*, 2464−2473.

(28) Hansen, V. Spectral Distribution of Solar Radiation on Clear Days: A Comparison Between Measurements and Model Estimates. *J. Clim. Appl. Meteorol.* **1984**, *23*, 772−780.

(29) Khantamat, O.; Li, C.-H.; Liu, S.-P.; Liu, T.; Lee, H. J.; Zenasni, O.; Lee, T.-C.; Cai, C.; Lee, T. R. Broadening the Photoresponsive Activity of Anatase Titanium Dioxide Particles via Decoration with Partial Gold Shells. *J. Colloid Interface Sci.* **2018**, *513*, 715−725.

(30) Vongsavat, V.; Vittur, B. M.; Bryan, W. W.; Kim, J.-H.; Lee, T. R. Ultrasmall Hollow Gold−Silver Nanoshells with Extinctions Strongly Red-Shifted to the Near-Infrared. *ACS Appl. Mater. Interfaces* **2011**, *3*, 3616−3624.

(31) Li, C.-H.; Li, M.-C.; Liu, S.-P.; Jamison, A. C.; Lee, D.; Lee, T. R.; Lee, T.-C. Plasmonically Enhanced Photocatalytic Hydrogen Production from Water: The Critical Role of Tunable Surface Plasmon Resonance from Gold−Silver Nanoshells. *ACS Appl. Mater. Interfaces* **2016**, *8*, 9152−9161.

(32) Ohtani, B. Titania Photocatalysis beyond Recombination: A Critical Review. *Catalysts* **2013**, *3*, 942−953.

(33) Khan, M. M.; Ansari, S. A.; Khan, M. E.; Ansari, M. O.; Min, B.-K.; Cho, M. H. Visible Light-Induced Enhanced Photoelectrochemical and Photocatalytic Studies of Gold Decorated SnO$_2$ Nanostructures. *New J. Chem.* **2015**, *39*, 2758−2766.

(34) Li, J.-M.; Cheng, H.-Y.; Chiu, Y.-H.; Hsu, Y.-J. ZnO-Au-SnO$_2$ Z-Scheme Photoanodes for Remarkable Photoelectrochemical Water Splitting. *Nanoscale* **2016**, *8*, 15720−15729.

(35) Li, Z.; Li, H.; Wu, Z.; Wang, M.; Luo, J.; Torun, H.; Hu, P.; Yang, C.; Grundmann, M.; Liu, X.; Fu, Y. Advances in Designs and Mechanisms of Semiconducting Metal Oxide Nanostructures for High-Precision Gas Sensors Operated at Room Temperature. *Mater. Horiz.* **2019**, *6*, 470−506.

(36) Chung, F.-C.; Wu, R.-J.; Cheng, F.-C. Fabrication of a Au@SnO$_2$ Core−Shell Structure for Gaseous Formaldehyde Sensing at Room Temperature. *Sens. Actuators, B* **2014**, *190*, 1−7.

(37) Rai, P.; Majhi, S. M.; Yu, Y.-T.; Lee, J.-H. Synthesis of Plasmonic Ag@SnO$_2$ Core−Shell Nanoreactors for Xylene Detection. *RSC Adv.* **2015**, *5*, 17653−17659.

(38) Song, H.-M.; Chon, B.-S.; Jeon, S.-H.; Rai, P.; Yu, Y.-T.; Dutta, P. K. Synthesis of Au@SnO$_2$ Core−Shell Nanoparticles with Controllable Shell Thickness and their CO Sensing Properties. *Mater. Chem. Phys.* **2015**, *166*, 87−94.

(39) Yu, Y.-T.; Dutta, P. Examination of Au/SnO$_2$ Core-Shell Architecture Nanoparticle for Low Temperature Gas Sensing Applications. *Sens. Actuators, B* **2011**, *157*, 444−449.

(40) Xu, C.; Tamaki, J.; Miura, N.; Yamazoe, N. Grain Size Effects on Gas Sensitivity of Porous SnO$_2$-based Elements. *Sens. Actuators, B* **1991**, *3*, 147−155.

(41) Wu, R.-J.; Lin, D.-J.; Yu, M.-R.; Chen, M. H.; Lai, H.-F. Ag@SnO$_2$ Core−Shell Material for Use in Fast-Response Ethanol Sensor at Room Operating Temperature. *Sens. Actuators, B* **2013**, *178*, 185−191.

(42) Zhang, J.; Liu, X.; Wu, S.; Xu, M.; Guo, X.; Wang, S. Au Nanoparticle-Decorated Porous SnO$_2$ Hollow Spheres: A New Model for a Chemical Sensor. *J. Mater. Chem.* **2010**, *20*, 6453−6459.

(43) Xu, F.; Ho, H.-P. Light-Activated Metal Oxide Gas Sensors: A Review. *Micromachines* **2017**, *8*, 333.

(44) Nagirnyak, S.; Dontsova, T. Effect of Modification/Doping on Gas Sensing Properties of SnO$_2$. *Nano Res. Appl.* **2017**, *03*. DOI: 10.21767/2471-9838.100025

(45) Suematsu, K.; Sasaki, M.; Ma, N.; Yuasa, M.; Shimanoe, K. Antimony-Doped Tin Dioxide Gas Sensors Exhibiting High Stability in the Sensitivity to Humidity Changes. *ACS Sens.* **2016**, *1*, 913−920.

(46) Aili, D.; Stevens, M. M. Bioresponsive Peptide−Inorganic Hybrid Nanomaterials. *Chem. Soc. Rev.* **2010**, *39*, 3358−3370.

(47) Li, C.-H.; Jamison, A. C.; Rittikulsittichai, S.; Lee, T.-C.; Lee, T. R. In Situ Growth of Hollow Gold−Silver Nanoshells within Porous Silica Offers Tunable Plasmonic Extinctions and Enhanced Colloidal Stability. *ACS Appl. Mater. Interfaces* **2014**, *6*, 19943−19950.

(48) Oldfield, G.; Ung, T.; Mulvaney, P. Au@SnO$_2$ Core−Shell Nanocapacitors. *Adv. Mater.* **2000**, *12*, 1519−1522.

(49) Choi, Y.-I.; Salman, S.; Kuroda, K.; Okido, M. Synergistic Corrosion Protection for AZ31 Mg Alloy by Anodizing and Stannate Post-Sealing Treatments. *Electrochim. Acta* **2013**, *97*, 313−319.

(50) Rai, D.; Yui, M.; Schaef, H. T.; Kitamura, A. Thermodynamic Model for SnO$_2$(cr) and SnO$_2$(am) Solubility in the Aqueous Na$^+$−H$^+$−OH$^-$−Cl$^-$−H$_2$O System. *J. Solution Chem.* **2011**, *40*, 1155.

(51) Hasani Bijarbooneh, F.; Zhao, Y.; Kim, J. H.; Sun, Z.; Malgras, V.; Aboutalebi, S. H.; Heo, Y.-U.; Ikegami, M.; Dou, S. X. Aqueous Colloidal Stability Evaluated by Zeta Potential Measurement and Resultant TiO$_2$ for Superior Photovoltaic Performance. *J. Am. Ceram. Soc.* **2013**, *96*, 2636−2643.

(52) Lee, S. H.; Hoffman, D. M.; Jacobson, A. J.; Lee, T. R. Transparent, Homogeneous Tin Oxide (SnO$_2$) Thin Films Containing SnO$_2$-Coated Gold Nanoparticles. *Chem. Mater.* **2013**, *25*, 4697−4702.

(53) Baur, W. H.; Khan, A. A. Rutile-Type compounds. IV. SiO$_2$, GeO$_2$ and a Comparison with Other Rutile-Type Structures. *Acta Crystallogr., Sect. B: Struct. Crystallogr. Cryst. Chem.* **1971**, *27*, 2133−2139.

(54) Xia, X.; Wang, Y.; Ruditskiy, A.; Xia, Y. 25th Anniversary Article: Galvanic Replacement: A Simple and Versatile Route to Hollow Nanostructures with Tunable and Well-Controlled Properties. *Adv. Mater.* **2013**, *25*, 6313−6333.

(55) Yallappa, S.; Manjanna, J.; Dhananjaya, B. L. Photosynthesis of Stable Au, Ag and Au-Ag Alloy Nanoparticles Using J. Sambac Leaves Extract, and their Enhanced Antimicrobial Activity in Presence of Organic Antimicrobials. *Spectrochim. Acta, Part A* **2015**, *137*, 236−243.

(56) Gržeta, B.; Tkalčec, E.; Goebbert, C.; Takeda, M.; Takahashi, M.; Nomura, K.; Jakšić, M. Structural Studies of Nanocrystalline SnO$_2$ Doped with Antimony: XRD and Mössbauer Spectroscopy. *J. Phys. Chem. Solids* **2002**, *63*, 765−772.

(57) Chen, Y.; Qu, B.; Mei, L.; Lei, D.; Chen, L.; Li, Q.; Wang, T. Synthesis of ZnSnO$_3$ Mesocrystals from Regular Cube-like to Sheet-like Structures and their Comparative Electrochemical Properties in Li-Ion Batteries. *J. Mater. Chem.* **2012**, *22*, 25373−25379.

(58) Kovacheva, D.; Petrov, K. Preparation of Crystalline ZnSnO$_3$ from Li$_2$SnO$_3$ by Low-Temperature Ion Exchange. *Solid State Ionics* **1998**, *109*, 327−332.

(59) Castillo-López, D. N.; Pal, U. Green Synthesis of Au Nanoparticles using Potato Extract: Stability and Growth Mechanism. *J. Nanopart. Res.* **2014**, *16*, 2571.

(60) Garbassi, F. XPS and AES Study of Antimony Oxides. *Surf. Interface Anal.* **1980**, *2*, 165−169.

(61) Volosin, A. M.; Sharma, S.; Traverse, C.; Newman, N.; Seo, D.-K. One-Pot Synthesis of Highly Mesoporous Antimony-Doped Tin Oxide from Interpenetrating Inorganic/Organic Networks. *J. Mater. Chem.* **2011**, *21*, 13232−13240.

(62) Jiang, Y.; Sun, W.; Xu, B.; Yan, M.; Bahlawane, N. Unusual Enhancement in Electrical Conductivity of Tin Oxide Thin Films with Zinc Doping. *Phys. Chem. Chem. Phys.* **2011**, *13*, 5760−5763.

(63) Pu, Y.-C.; Chen, Y.-C.; Hsu, Y.-J. Au-Decorated $Na_xH_{2−x}Ti_3O_7$ Nanobelts Exhibiting Remarkable Photocatalytic Properties under Visible-Light Illumination. *Appl. Catal., B* **2010**, *97*, 389−397.

(64) Fan, L.; Tang, L.; Gong, H.; Yao, Z.; Guo, R. Carbon-Nanoparticles Encapsulated in Hollow Nickel Oxides for Super-capacitor Application. *J. Mater. Chem.* **2012**, *22*, 16376−16381.

(65) Jacob, A. A.; Balakrishnan, L.; Shambavi, K.; Alex, Z. C. Multi-Band Visible Photoresponse Study of Co^{2+} Doped ZnO Nano-particles. *RSC Adv.* **2017**, *7*, 39657−39665.

(66) Zhu, H.; Tao, J.; Dong, X. Preparation and Photo-electrochemical Activity of Cr-Doped TiO_2 Nanorods with Nano-cavities. *J. Phys. Chem. C* **2010**, *114*, 2873−2879.

(67) Maeda, K.; Domen, K. Preparation of $BaZrO_3$−$BaTaO_2N$ Solid Solutions and the Photocatalytic Activities for Water Reduction and Oxidation under Visible Light. *J. Catal.* **2014**, *310*, 67−74.

(68) Ganose, A. M.; Scanlon, D. O. Bandgap and Work Function Tailoring of SnO_2 for Improved Transparent Conducting Ability in Photovoltaics. *J. Mater. Chem. C* **2016**, *4*, 1467−1475.

(69) Dou, M.; Persson, C. Comparative Study of Rutile and Anatase SnO_2 and TiO_2: Band-Edge Structures, Dielectric Functions, and Polaron Effects. *J. Appl. Phys.* **2013**, *113*, 083703.

(70) Lu, P.-F.; Shen, Y.; Yu, Z.-Y.; Zhao, L.; Li, Q.-Y.; Ma, S.-J.; Han, L.-H.; Liu, Y.-M. Electronic Structure and Optical Properties of Antimony-Doped SnO_2 from First-Principle Study. *Commun. Theor. Phys.* **2012**, *57*, 145−150.